11134 *Biochemistry* **2009,** *48,* 11134–11141
DOI: 10.1021/bi9001425

BIOCHEMISTRY
including biophysical chemistry & molecular biology
Article

2.6 Å X-ray Crystal Structure of Human p53R2, a p53-Inducible Ribonucleotide Reductase[†,‡]

Peter Smith,[§,#] Bingsen Zhou,[⊥,#] Nam Ho,[∥] Yate-Ching Yuan,[@] Leila Su,[@] Shiou-Chuan Tsai,[*,§,Δ] and Yun Yen[*,⊥]

[∥]*Department of Molecular Biology and Biochemistry,* [§]*Department of Chemistry, and* [Δ]*Department of Pharmaceutical Sciences, University of California, Irvine, California 92697.* [⊥]*Department of Clinical and Molecular Pharmacology and* [@]*Bioinformatics Core, City of Hope National Medical Center, 1500 East Duarte Road, Duarte, California 91010* [#]*These authors contributed equally to this work.*

Received January 28, 2009; Revised Manuscript Received September 3, 2009

ABSTRACT: Human p53R2 (hp53R2) is a 351-residue p53-inducible ribonucleotide reductase (RNR) small subunit. It shares >80% sequence identity with hRRM2, the small RNR subunit responsible for normal maintenance of the deoxyribonucleotide (dNTP) pool used for DNA replication, which is active during the S phase in a cell cycle-dependent fashion. But rather than cyclic dNTP synthesis, hp53R2 has been shown to supply dNTPs for DNA repair to cells in G0-G1 in a p53-dependent fashion. The first X-ray crystal structure of hp53R2 is determined to 2.6 Å, in which monomers A and B exhibit mono- and binuclear iron occupancy, respectively. The pronounced structural differences at three regions between hp53R2 and hRRM2 highlight the possible regulatory role in iron assimilation and help explain previously observed physical and biochemical differences in the mobility and accessibility of the radical iron center, as well as radical transfer pathways between the two enzymes. The sequence−structure−function correlations that differentiate hp53R2 and hRRM2 are revealed for the first time. Insight gained from this structural work will be used in the identification of biological function, regulation mechanism, and inhibitor selection in RNR small subunits.

RNR[1] catalyzes the reduction of all four ribonucleotides to their corresponding deoxyribonucleotides, the building blocks for DNA biosynthesis (*1*). There are currently three identified classes of RNRs. Class I RNRs are biologically active as $\alpha_2\beta_2$ tetramers. Three class I RNR subunits have been identified in mammals. The large (α) subunit, M1, contains the enzyme active site and allosteric effector sites where substrate reduction is mediated by a cysteine thiyl radical, and a pair of redox active cysteines (*1*). The small (β) subunit, M2, contains a dinuclear iron site that instigates formation of a stable tyrosyl radical via the four-electron reduction of molecular oxygen to water (*2*, *3*). The hRRM2−M1 holo complex provides dNTPs to proliferating cells in an S phase-dependent fashion (*4*), where hRRM2 is under the transcriptional regulation of cell cycle-associated factors (*5*−*7*). p53R2, identified in 2000 by Tanaka et al., is a small subunit exhibiting many conserved features of M2 (>80% identical). Like M2, p53R2 contains the diiron/dityrosyl cofactor, but p53R2, and not M2, is transactivated by p53 in response to DNA damage to cells in G0-G1 in a p53-dependent fashion (*8*, *9*). Additionally, p53R2-null mice demonstrated an enhanced frequency of spontaneous mutations and activation of p53-dependent apoptotic pathways (*10*). The hp53R2 gene contains a 20-nucleotide p53 binding site in intron 1, and two putative stretches of nuclear localization sequences on the gene product (*8*). Both hRRM2 and hp53R2 were shown to interact with hRRM1 through the C-terminal binding domain and converted CDP to dCDP (*11*). Further, the highly conserved diiron/dityrosyl pockets afford both hp53R2 and hRRM2 the ability to form the tyrosyl radical necessary for NDP reduction at hRRM1 (*12*, *13*). Despite the high degree of sequence identity, hRRM2 and hp53R2 exhibit many differences that are reflected in their different biological roles in assisting DNA biosynthesis in two distinct pathways described above. The hRRM2 crystal structure is available (PDB entry 2UW2). However, past attempts to identify compounds that selectively inhibit either hRRM2 or hp53R2 have been severely hampered by the lack of the hp53R2 crystal structure. In this work, we present the 2.6 Å X-ray crystal structure of hp53R2, the first X-ray crystal structure of a human p53R2 enzyme. Extensive structural comparisons between hp53R2 and other mammalian R2s offer a high-resolution rationale for differences in susceptibilities to iron extruding and radical scavenging agents.

MATERIALS AND METHODS

Materials. All chemicals were purchased from Sigma-Aldrich Chemical Co. and were the highest grade available. pET28a(+) from *Escherichia coli* strain BL21(DE3) was purchased from Novagen.

[†]This work was supported partially by National Cancer Institute Grant CA 127541 and the Sino-American Cancer Foundation.

[‡]The atomic coordinates have been deposited in the Protein Data Bank (PDB) as entry 3HF1.

*To whom correspondence should be addressed. Y.Y.: Department of Clinical and Molecular Pharmacology, City of Hope National Medical Center, 1500 E. Duarte Rd., Duarte, CA 91010; phone, (626) 256-4673, ext. 65707; fax, (626) 471-7204; e-mail, yyen@coh.org. S.-C. T.: Department of Molecular Biology and Biochemistry, Department of Chemistry, and Department of Pharmaceutical Sciences, University of California, Irvine, California 92697. phone, (949) 824-4486; fax, (949) 824-8552; e-mail, sctsai@uci.edu.

[1]Abbreviations: RNR, ribonucleotide reductase; M1, human ribonucleotide reductase large subunit; M2, human ribonucleotide reductase small subunit; NDP, nucleoside diphosphate; NTP, nucleoside triphosphate; CDP, cytidine 5′-diphosphate; dNDP, deoxynucleoside diphosphate; dNTP, deoxynucleoside triphosphate; MR, molecular replacement; SA, simulated annealing.

 Published on Web 09/03/2009

Protein Expression and Purification. His_6-tagged hp53R2 was expressed as previously reported (*13*); the purification was modified as follows. All steps were performed at 4 °C. Harvested cells were suspended in lysis buffer [Tris (pH 7.5), 150 mM NaCl, 50 mM imidazole, and 10% glycerol], sonicated, and clarified. This was followed by TALON metal affinity resin purification. The partially purified protein was concentrated to 10 mg/mL and further purified by gel filtration on a Superdex 200 HR 10/300 GL column with 20 mM Tris (pH 7.5) and 150 mM NaCl to afford >99% pure protein.

Crystallization and Data Collection. hp53R2 was crystallized via the sitting drop vapor diffusion method at 25 °C. Two microliters of 4.5 mg/mL protein in 20 mM Tris (pH 7.5) with 150 mM NaCl was added to 2 μL of precipitant [0.1 M sodium citrate (pH 6.45), 1.3 M Li_2SO_4, and 0.5 M $(NH_4)_2SO_4$]. The reservoir volume was 250 μL. Crystals were visible after 7 days, with the full size reached between 10 and 14 days. Ferrous ammonium sulfate was added to crystal drops for a final concentration of 5 mM 1 h prior to harvesting. Prior to being flash-cooled with liquid N_2, crystals were cryoprotected in a 70:30 (v/v) solution of crystallization precipitant and glycerol. A 2.6 Å resolution data set was collected at the Advanced Light Source (ALS, beamline 8.2.1) at −160 °C. A 3.4 Å SAD data set was collected at the Fe peak (1.74 Å) after observation of a strong iron fluorescence signal to confirm the presence of iron. All data were processed with HKL2000 (*14*). Statistics for both data sets are listed in Table S1 of the Supporting Information.

Structure Determination. The structure of hp53R2 was determined via MR using the mouse R2 structure (PDB entry 1XSM) (*15*) as a template with EPMR (*16*). Refinement began with CNS (*17*) using torsion angle SA followed by energy minimization, with positional and individual *B*-factor refinement. Subsequent iterative rounds of model rebuilding with (Win) Coot (*18*) and refinement in CNS with the maximum likelihood approach were used to lower the free and crystalline *R* values. Finally, waters and crystallization agents were added to nonprotein density.

Iron Sites. Upon synchrotron irradiation of the crystal (back-soaked in iron-free cryoprotectant prior to being frozen) at the iron absorption edge, a strong fluorescence signal was detected. Two large anomalous peaks were observed from the anomalous difference map (FT (fom (|f_a + |-|f_a-|) exp(i[phase-90]) calculated using CNS (*17*), with the SAD experimental amplitudes (1.74 Å) (Table S1 of the Supporting Information). The model phase calculated from the refined hp53R2 model was used. A simulated annealing composite omit map was subsequently generated by CNS that corroborated the peak from the anomalous FT map with a defined patch of electron density outside the current protein model, and overlaying right on the highest anomalous difference peaks (8.92 and 6.93 I/σ, respectively) that are positioned at the expected iron-coordinating residues, where iron is expected to bind hp53R2 by homology to the mRRM2 coordinates. The monomer B Fe1 and Fe2 sites were treated as two separate iron atoms and refined, with energy minimization followed by positional and individual *B*-factor refinement settings. Iron occupancies were set to 1 for both Fe2 sites, and the individual *B*-factors were refined to 60.77 for Fe2 in monomer A and 82.11 for Fe2 in monomer B. The iron occupancy of Fe1 in monomer B was refined to 0.45 and the individual *B*-factor to 79.07. Upon removal of the iron coordinates from the refined structure, as well as calculation of a composite omit map and an $F_o - F_c$ map, a patch of robust electron density is observed at the Fe1 site (composite omit map contoured at 1.0σ and $F_o - F_c$ map contoured at 3.0σ). These data are further corroborated by the anomalous difference map, which displays clear density overlapping the same vicinities (strong density contoured at 3.0σ).

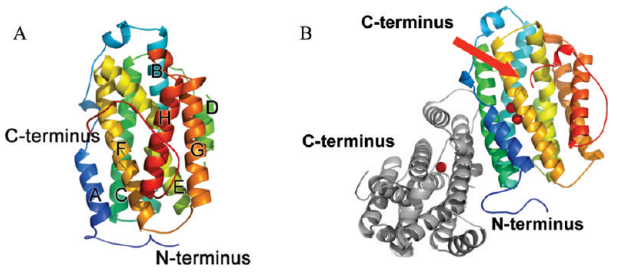

FIGURE 1: (A) Overall topology of hp53R2 monomer B. The structure is entirely helical [helices A−H as described previously (*15*)], beginning at residue S29 and ending at residue L317. The helices form a central helical bundle around the dityrosyl/diiron active site, for which structural details are described in the text. (B) Overall dimer showing monomer B in an orientation similar to that of panel A, along with iron sites, and monomer A (gray). The lower iron in the image is Fe1.

RESULTS AND DISCUSSION

Overall Fold. The hp53R2 structure was resolved to 2.6 Å and refined to an R_{crys} of 22.2% (R_{free} = 27.3%). The natural dimer is observed per asymmetric unit (Figures 1B and S5). The coordinates exhibit a topology highly similar to those of hRRM2 (PDB entry 2UW2, pending publication with coordinates released) and mRRM2 structures (PDB entries 1XSM, 1W68, and 1W69) (*15*, *19*). The structure also maintains a similar pattern of disorder at the N- and C-termini. The structure consists of helices and loops, and 8 of the 11 helices form a central bundle, for which a secondary structure identification scheme has been described with the mRRM2 structure (Figure 1A) (*19*). Both monomers of hp53R2 can be superimposed onto mRRM2 and hRRM2 with a root-mean-square deviation (rmsd) of 0.80−0.93 Å. The two monomers in hp53R2 have a 0.69 Å rmsd. The electron density map for monomer A has gaps (missing both backbone and side chain density) from position 1 to 28, from position 101 to 104, and from position 312 to 351, while in monomer B, there are gaps from position 1 to 29, from position 160 to 161, and from position 318 to 351. Additionally, though the backbone density is clear, D100 of monomer B is missing side chain density.

Iron Site: Mono- versus Diiron in Monomers A and B. The hp53R2 iron-binding site is created by α-helices B, C, E, and F, as in the mRRM2 and hRRM2 structures (Figure 1A,B) (*15*, *19*). However, the active site iron coordination environment (E131, H134, D100, E194, E228, and H231) is different between monomers A and B (Figure 2A−D). Monomer A exhibits one iron in the active site (Fe2 by convention), whereas monomer B exhibits occupancy of both iron sites. The Fe sites were confirmed to be iron on the basis of a SAD data set collected at the iron absorption peak (1.74 Å). The two highest peaks in the anomalous Fourier map correspond to one of the two previously reported iron locations, Fe2, in both monomers A and B (Figure 2C). In monomer B, the second iron site (Fe1 by convention) is also observed in an $F_o - F_c$ omit map (Figure 2B). In the Fourier transform electron density map, the monomer B Fe1−Fe2 density appears as two overlapping distorted spheres over a much larger region than would be expected for a single iron (Figure 2C). The 3.5 Å resolution of the SAD data set may be too

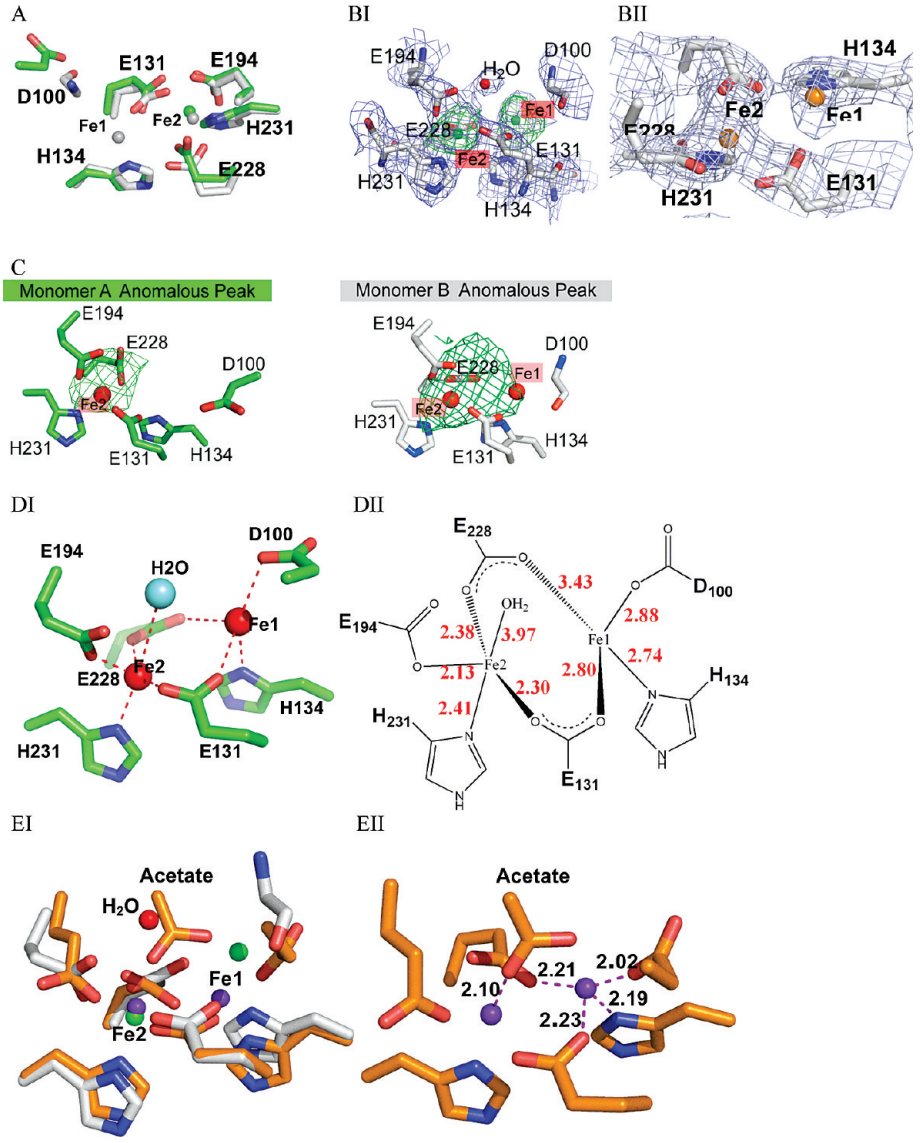

FIGURE 2: (A) Overlay of monomer A (green) and monomer B (gray) iron coordination sites. Subtle shifts in the positions of all residues and a dramatic shift in the position of the D100 backbone. (BI) Electron density of iron coordination residues in monomer B. Blue density is the $2F_o - F_c$ map contoured at 1σ. Green spheres around iron sites show the $F_o - F_c$ omit map contoured at 3σ. (BII) Composite omit map, contoured at 1σ, calculated after removal of the iron atoms from the model to show the Fe1 density. (C) Anomalous difference peaks of iron atoms, calculated with refined model phase and the 3.5 Å SAD (1.74 Å) amplitudes. Electron density is contoured at 3.0σ. (DI) Irons and coordination residues and/or water in monomer B. (DII) Schematic displaying the same environment as and an orientation similar to that in panel DI, with distances (angstroms). The D100 side chain is hypothetical (logical stereochemical and conformational constraints) as it is not seen in the electron density. (EI) Overlay of reduced mRRM2 (PDB entry 1W69) colored orange and hp53R2 monomer B colored gray to show significant positional differences among many of the active site residues (orientation similar to that of the images in panel D). (EII) Image displaying iron coordination distances (angstroms) for 1W69 to highlight where they are substantially different between the active sites of hp53R2 and 1W69 (orientation similar to that of images in panel D; coordination distances can be compared to those of hp53R2 in panel DII). Water·hp53R2 structure; acetate·mRRM2 structure. hp53R2 irons, green; mRRM2 irons, purple.

low to resolve the distance between the two iron sites. As found in the $F_o - F_c$ omit map (Figure 2B), these atoms are approximately 5 Å apart. The active site iron coordination environment (E131, H134, D100, E194, E228, and H231) is different between monomers A and B (Figure 2A–D). This reflects the mono- and diiron occupancies in monomers A and B, respectively. This crystal structure captures the mono- or diiron occupied hp53R2 for the first time.

Shifted Fe1 Position. The superposition of Fe1–Fe2 sites in hp53R2 monomer B and mRRM2 (PDB entry 1W69, also with two Fe sites) suggests that the irons are under a reducing condition due to the lack of oxide density in the putative μ-oxo iron bridge position (Figure 2E) (*15*). This could be a result of the excess Fe^{II} in the crystallization drop. The reduced active site is not the enzymatically active form of the enzyme. The active subunit is the diferric form in which the active tyrosyl radical is created via the following reaction:

$$(\text{apo})\text{R2} + 2\text{Fe}^{\text{II}} + 4\text{e}^- + \text{O}_2 + 2\text{H}^+ \rightarrow (\text{Fe}^{\text{III}} - \text{O} - \text{Fe}^{\text{III}}/\text{Y}^{\bullet})\text{R2} + \text{H}_2\text{O}$$

where the first three reducing electrons are iron-derived and the fourth is from oxidation of the active tyrosine. Just as in the two monomers of hp53R2, the major observable difference between the hp53R2 and hRRM2 active sites is the position of hp53R2 D100 relative to D138 of hRRM2, as well as the position of Fe1

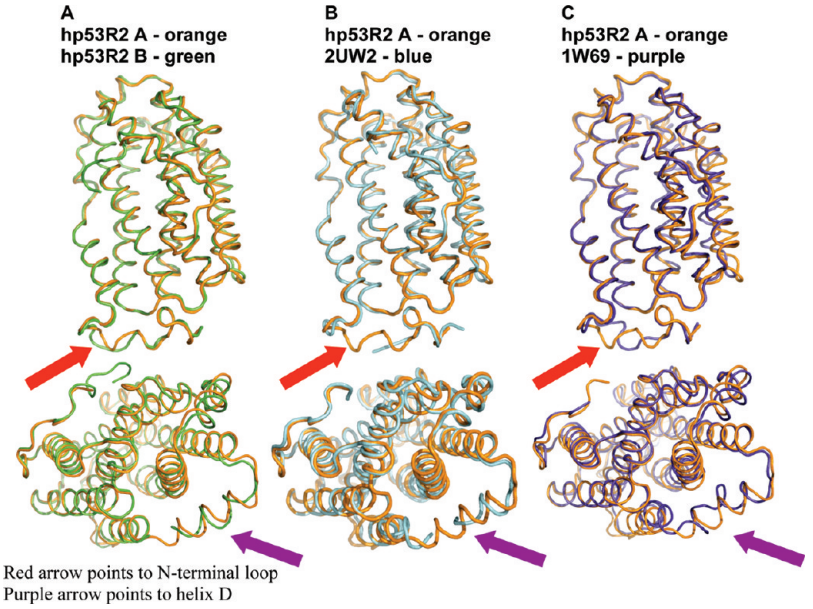

FIGURE 3: (A) C_α overlay of hp53R2 monomer A (orange) and hp53R2 monomer B (green) with an orientation similar to that of Figure 1. The N-terminus and helix G display clear conformational differences between the monomers and are the regions of greatest structural difference between the homologues as shown in panels B and C. (B) C_α overlay of hp53R2 monomer A and hRRM2 (PDB entry 2UW2). (C) C_α overlay of hp53R2 monomer A and mRRM2 (PDB entry 1W69).

(Figure 2E). hp53R2 monomer B exhibits electron density for the main chain atoms of D100, though no side chain density could be observed for monomer B at residue 100 (thus, a glycine is included at this position for monomer B in Figure 2A−C,E). Figure 2D displays a hypothetical positioning of the D100 side chain in monomer B based on stereo and conformational constraints, and logical orientation with regard to the Fe1 site. High D100 flexibility in this environment could be the reason for the shift of the Fe1 site (Figure 2D,E). For example, mRRM2 E170 is 2.03 Å from the Fe1 iron site, while the corresponding hp53R2 E131 is 2.80 Å from the Fe1 iron position in hp53R2 monomer B (Figure 2D,E). Further, hp53R2 H134 is 2.74 Å from the same site, while the corresponding mRRM2 H173 is only 2.19 Å from the mouse Fe1 iron position. From in vitro biochemical studies, hp53R2's diferric iron center was 158-fold more susceptible to the iron chelator deferoxamine mesylate than hMMR2 was and 2.5 times less sensitive than hRRM2 to the radical scavenger hydroxyurea (*10*). In addition, the bivalency of E228 in hp53R2 is not observed in mRRM2 or hRRM2 (*15*, *19*). These observations, taken with the structural details, lead to a proposal that there are differences in gating capabilities and mechanisms regarding iron assimilation and susceptibilities to radical scavenging agents between hp53R2 and other mammalian RRM2s. For the sake of clarity, Figure 3 (overlays of C_α traces) is provided to highlight the regions with the most substantial differences between hp53R2 and different RRM2 structures.

Structural Basis of B Helix Disorder: The N-Terminal Swivel Region. The crystal exhibits the dimer per asymmetric unit. To verify that this structure contains the true biological unit, we have provided an FPLC trace from a gel filtration result (Figure S5 of the Supporting Information), and we extend a comparison of hp53R2 to the *E. coli* X-ray crystal structure, both in the Supporting Information. Similarly, use of the homologous structure dimers is described in the Supporting Information. The hp53R2 structure offers two snapshots of the protein conformation trapped in mono- and diiron occupancies for monomers A and B, respectively (Figure 4A). N-Terminal residues 37−42 from one monomer can swivel between two conformations and impose significant influences on helix D (Figure 4F,G) and helix B of the opposite monomer (Figure 4D,E). This change ultimately affects the orientation of D100 and, thus, the integrity of the binuclear iron environment (Figure 4A). Specifically, D100 in monomer A is swung away from the active site, compared to monomer B (D100 side chain in monomer B artificially modeled in image 2D; it is not actually in the density map). In the deposited structure, only the backbone density is modeled, as displayed in all other panels of Figure 2. Note that though the side chain for D100 in monomer B is missing, we do clearly see the backbone density. Because there is clear electron density of both backbone and side chain density from D101 to D104 in monomer B, the difference in the D100 main chain position between monomers A and B would create a different environment in this region. We will refer to the N-terminal residues (residues 37−42) as the N-terminal swivel region throughout this work.

Upon examination of the N-terminal swivel region in Figure 4C, in hp53R2 monomer A, R41 is swung inward by ~90° from its position in monomer B (i.e., it interacts with the same monomer) and forms a salt bridge with the E119 side chain of monomer A. In this conformation, F42 is flipped inward and R40 of monomer A is swung outward to form a hydrogen bond with G101 in monomer B (4.05 Å from G101) (Figure 4E). Furthermore, K37 in monomer A spans the dimer interface to form a salt bridge with E105 to stabilize helix B of monomer B. The interactions of the monomer A N-terminal swivel region stabilize the B-helix of monomer B and allow D100 of monomer B to be oriented in the proper vicinity to bind iron (Fe1), thereby stabilizing the full binuclear iron environment. Conversely, in the N-terminal swivel region of monomer B, R40 flips inward and forms a hydrogen bond with the E119 side chain, F42 flips outward and interrupts helix B, and D100 no longer interacts favorably with the iron center (Figure 4D). Therefore, interactions of the N-terminal residues in monomer B with the B-helix in monomer A are correlated with the helix B disorder, which

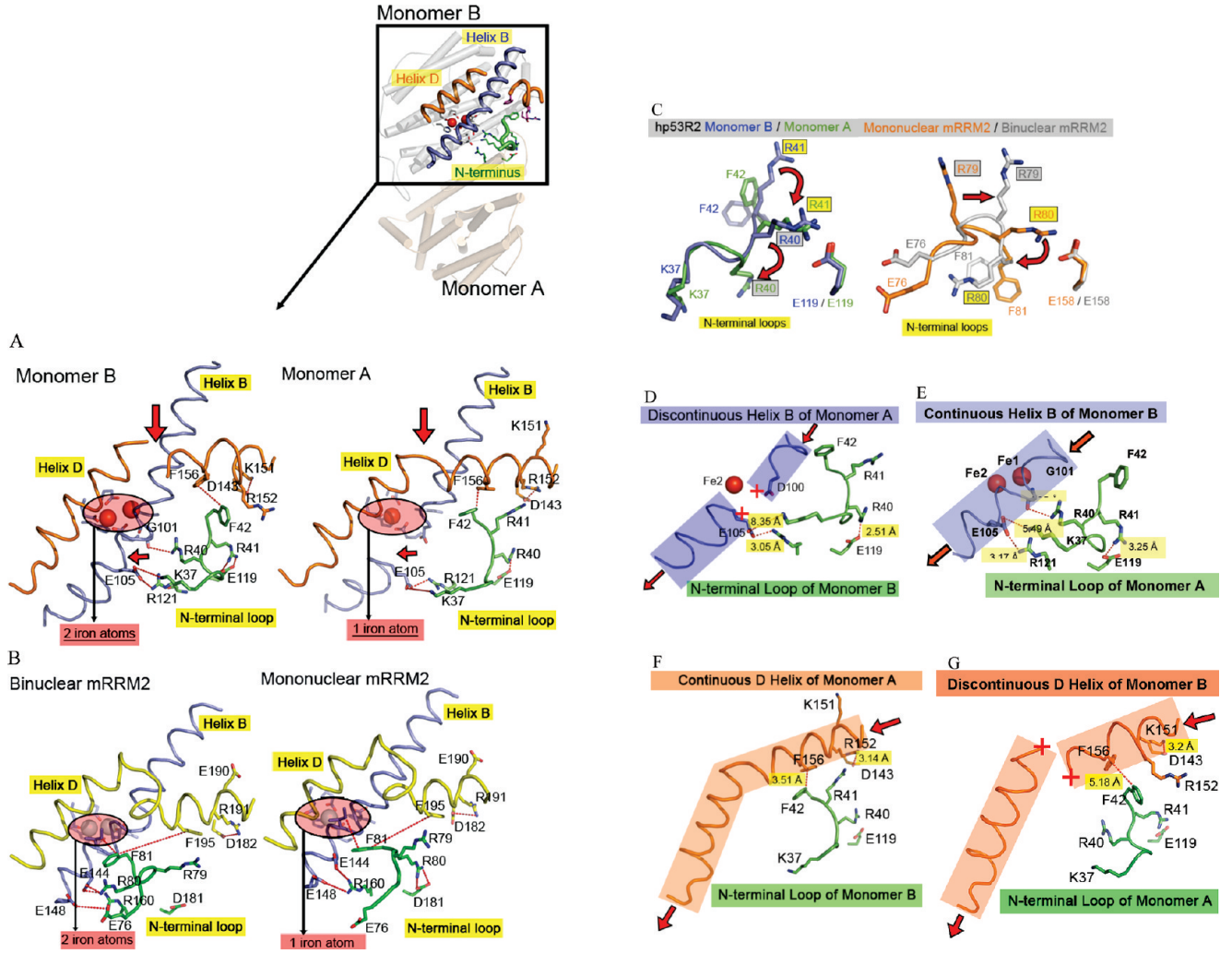

FIGURE 4: (A) Bird's eye view of the N-terminal swivel region and secondary structure regions it contacts within the hp53R2 dimer, and also zoom views of monomers A and B. Major conformational differences highlighted with red arrows, and highlighted iron atoms. (B) The homologous structural regions as in panel A, but for mouse structures 1W69 (left) and 1XSM (right). (C) Residues of the N-terminal swivel region, overlaying hp53R2 monomers A and B (left), and mRRM2 mononuclear (1XSM) and binuclear occupied iron (1W69) structures (right). The major conformational changes for the sequence-identical Arg residues are denoted with red arrows. (D) Interactions between the monomer B N-terminal swivel region and monomer A (helix B) that lead to destabilization of helix B, and ultimately mononuclear iron occupancy. Red arrows indicate directionality of helix. (E) Interactions between the monomer A N-terminal swivel region and monomer B (helix B) that lead to stabilization of helix B, and ultimately binuclear iron occupancy. Red arrows indicate the directionality of the helix. For the sake of clarity, a water molecule was left out of this panel. There is a water spanning the gap between the Lys37 ammonium of monomer A and E105 of helix B on monomer B (2.34 Å from Lys37 to the water and 3.20 Å from the water to the carboxylate of E105). (F) Interactions between the monomer B N-terminal swivel region and helix D of monomer A that stabilize helix D. Additionally highlighted is the salt bond between R152 and D143 in the D-loop region that exists in the stabilized D-helix conformation. Red arrows indicate the directionality of the helix. (G) Interactions between the monomer A N-terminal swivel region and helix D of monomer B that destabilize helix D. Additionally highlighted is the salt bond between K151 and D143 in the D-loop region that exists in the destabilized D-helix conformation. Red arrows indicate the directionality of the helix.

presumably prevents D100 of monomer A from binding the second Fe.

hp53R2 Helix D and D-Loop. The N-terminal swivel region also affects the order at helix D. As seen in Figure 4F, when R40 forms a bridge to E119 of monomer B, F42 is positioned 3.51 Å from F156 on helix D of monomer A, forming a hydrophobic interaction. With this interaction intact, the remainder of helix D is ordered. As seen in Figure 4G, when R41 forms a bridge to E119 of monomer A, F42 is now flipped 5.18 Å from F156 of helix D on monomer B and no longer creates a favorable hydrophobic interaction. The loss of this Phe−Phe interaction is concurrent with the loss of order in the middle of helix D (missing E160 and T161).

The third structural region affected by the two N-terminal swivel conformations is the D-loop (residues D143−R152). As seen in Figure 4F, when F42 stacks with F156 of monomer A, R152 forms a bridge to D143 with a distance of 3.14 Å and K151 is facing solvent. The R152−D143 salt bridge exists when there is order in helix D. The alternative conformation is seen in Figure 4G, where no favorable hydrophobic interaction is maintained between F42 of monomer A and F156 of monomer B. This translates to the K151 of monomer B forming a bridge to D143 with a distance of 3.2 Å, and R152 is facing solvent. The K151−D143 salt bridge coincides with the disorder of helix D.

mRRM2 N-Terminal Swivel on Helices B and D and the D-Loop. Unlike the hp53R2 N-terminal swivel region, in the mRRM2 swivel, only R80 (equivalent to hp53R2 R41) adopts two different conformations (Figure 4C). R79 merely shifts a small distance and does not create any new interactions. As in hp53R2, F81 of mRRM2 also flips between two conformations.

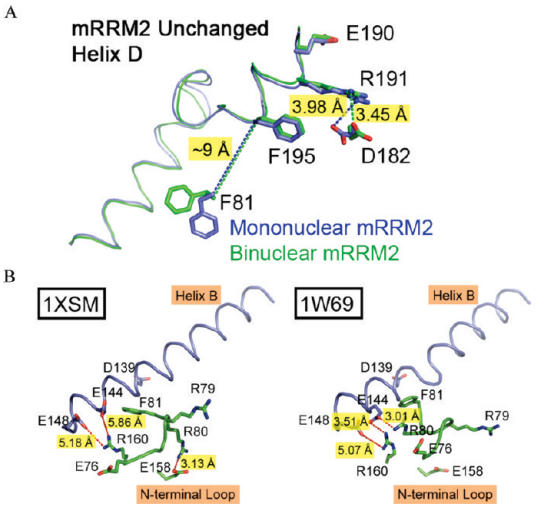

FIGURE 5: (A) Overlay of D-helix regions of both mono- and binuclear occupied mRRM2 structures (PDB entries 1XSM and 1W69) highlighting the lack of conformational change between the two, due to the lack of cross talk between the F81 residues at the N-terminal swivel regions of the structures. (B) Comparison of the interactions between the N-terminal swivel region and the B-helix of both structures. Structural integrity of helix B is preserved in both mono- and binuclear occupied structures, because the N-terminal swivel region does not impose sufficiently strong differences from one swivel conformation to the other in its interactions with helix B.

The N-terminal swivel region on the hRRM2 structure is likely similar to the same region on the mRRM2 structure, where the coordinates (PDB entry 2UW2) for this region (residues 78−81) are missing. For the sake of clarity, this region is highlighted in Figure 3, identifying it as one of the two regions where the most differences are seen between hp53R2 and m/hRRM2.

Helix B in each of the mononuclear and binuclear iron-occupied mRRM2 structures is ordered (Figure 5B). When R80 forms a bridge to E144, it aids in pulling the N-terminus and helix B closer together (Figure 5B, PDB entry 1W69) where, in addition to this salt bridge, R160 is brought closer to E144 and E148 by 2.35 Å (5.86 − 3.51 = 2.35) and 0.11 Å (5.18 − 5.07 = 0.11), respectively. E76 in mRRM2 cannot create any favorable interactions with E144 or E148 on helix B. In contrast, hp53R2 has K37 (the residue equivalent to E76 in mRRM2), which forms a salt bridge with E105 on helix B, resulting in the disordered helix B in monomer A (Figure 4D).

As seen in Figure 4B, helix D in each of the mononuclear and binuclear iron occupied mRRM2 structures is ordered. Figure 5A displays the overlaid "would-be" interacting residues between the N-terminal swivel region and helix D of both mRRM2 structures. In both mRRM2 structures, F81 and F195 (equivalent to F42 and F156 of hp53R2, respectively) are ~9 Å apart and form no hydrophobic interactions. Therefore, the N-terminal swivel region of mRRM2 does not dictate the conformational change or order at helix D. As for the D-loop conformation, K151 and R152 in hp53R2 are equivalent to E190 and R191 in mRRM2, respectively. In comparison, both mono- and diiron mRRM2 structures (Figure 5A) show that the D-loop (residues 182−190) has only one conformation, where R191 forms a bridge to D182.

hp53R2/mRRM2 N-Terminal Swivel Region Comparative Summary. The N-terminal swivel region and its two conformations in the hp53R2 (monomer A vs B) and mRRM2 (mono-Fe vs di-Fe) structures showed that the N-terminal region communicates directly with three different regions (helix B, D-loop, and helix D) on the opposite monomer (Figure 4A,B). Through F42−F156 hydrophobic interaction, the N-terminal swivel region can stabilize or destabilize helix D in hp53R2, but not in mRRM2 (Figure 4F,G and Figure 5A). In addition to the lack of Phe−Phe communication between the N-terminal swivel region of mRRM2 and the D-helix, the lack of K151 in mRRM2 (which has an E190 at this position) also precludes mRRM2 from forming the swivel at the D-loop. Only in hp53R2 do the two swivel conformations lead to a significant effect at helix B. This difference is essentially due to the sequence variation between K37 in hp53R2 and its sequence equivalent E76 on mRRM2.

When synthesizing all these components, we find it is clear that hp53R2 has more cross talk between its secondary structural regions than its eukaryotic counterparts, because of unique swivel points and favorable charge interactions. These regions work to either open or close helix B, a motion that acts as a gatekeeper to the iron coordination environment. The fact that helix B can exist in an open conformation in hp53R2 not only implies a different mechanism of incorporation of iron from homologous RRM2 structures but also is consistent with the observation that hp53R2 binds iron less well, and that it is more susceptible to the iron chelating deferoxamine mesylate (*13*). We propose this to be a unique gating mechanism for allowing iron in and out of the hp53R2 active site. This is also corroborated by the observation that hp53R2 is 158-fold more susceptible to iron extrusion by deferoxamine mesylate than hRRM2 (*13*). A main point to be clarified is that, though both mRRM2 structures maintain order at helix B, only one exhibits binuclear iron occupancy. The mononuclear iron occupied mRRM2 was crystallized at pH 4.7; even though the structural integrity might allow for residence of both iron sites, iron is acid labile, and the condition is too acidic.

Additional Attributes of Helix D, Cys versus Tyr. As an integral part of the gating mechanism, helix D can adopt two conformations in hp53R2, but not in mRRM2. Looking from a bird's eye view of helix D (Figure 6A), we find that in hp53R2 it maintains a regular helical order but is bent in the middle, in hRRM2 this region has more looplike characters than α-helices, and in mRRM2 it has an additional kink. The variation of this topology goes beyond the previous discussion of helix D and looks farther down the helix in the C-terminal direction, where a critical sequence variation of C203/202 in m/hRRM2 is equivalent to Y164 in hp53R2 (Figure 6B). When the structures overlap, the cysteine C_α atom in hRRM2 is 5 Å from the C_α atom of hp53R2 Y164, which forms a 2.86 Å hydrogen bond with E262 (Figure 6B). Because m/hRRM2 has a Cys instead of a Tyr at this position, this H-bond does not occur in the RRM2 structures. Rather, K206 of the RRM2 structures forms a salt bridge with the sequence equivalent glutamate (E300). Y164 in hp53R2 also forms π-stacking interactions with F265 that do not occur in the RRM2 structures (Figure 6B). The interactions mediated by Y164 of hp53R2 bring helix D and helix G closer together in hp53R2 than they do in RRM2 structures. As K206 of the RRM2 structures reaches to bridge E300, thereby occupying the space where a tyrosine would sit, it kinks the helix and leads to the helix D conformation seen in Figure 6A. The sequence equivalent K168 in hp53R2 does not form this salt bridge, because Y164 bonds with E262, though K168 still forms a hydrogen bond with Y164 (Figure 6B).

The switch from a Cys in the RRM2 structures to a Tyr in hp53R2 leads to a major structural difference: hp53R2 has an

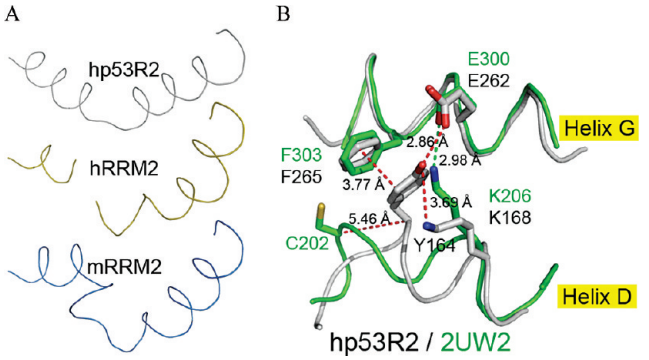

FIGURE 6: (A) Overlaid stretch of helix D residues from identical vantage points of homologous structures: hp53R2 monomer A, hRRM2 (PDB entry 2UW2), and mRRM2 (PDB entry 1XSM) (from top to bottom). (B) hp53R2 structure colored gray and hRRM2 colored green. The switch from hRRM2 C202 to hp53R2 Y164 at this sequence equivalent position confers dramatic conformational changes among the compared structures, because of different noncovalent interactions that can or cannot happen in hp53R2 vs hRRM2. Y164 forms a hydrogen bond to E262, and thus, K168 does not form a salt bond there. In contrast, in the hRRM2 structure, K206 (sequence equivalent of hp53R2 K168) forms a salt bridge with the equivalent glutamate (E300). The conformation of all mRRM2 structures is nearly identical at the displayed positions in the 2UW2 coordinates; therefore, only hRRM2 is depicted for comparison to hp53R2.

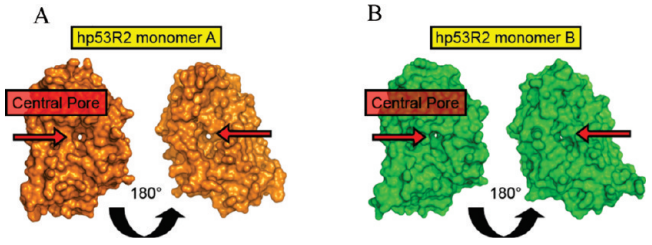

FIGURE 7: (A) Surface representations displaying identical vantage points and 180° rotations of hp53R2 monomers A and B. hp53R2 exhibits a hole proximal to the iron coordination site that traverses the entire structure, which is not seen in the compared structures (see Figure S2 of the Supporting Information for hRRM2 and mRRM2 surface representations).

open channel (Figure 7A,B) in RRM2 never previously reported. This open channel helps explain why hp53R2 has iron chelator susceptibilities drastically different from those of hRRM2. Both hp53R2 monomers have an opening that runs through the Fe2 site; the Fe1 site in monomer B also resides in this open channel (Figure S1B−D of the Supporting Information). At the surface, h- and mRRM2 have F237 and F236, respectively, that correspond to hp53R2 F198 (Figure 7A). However, in hp53R2, Y164 spans helices D and G and alters the conformations of a series of Phe residues, ultimately moving them out of the vicinity of the pore. Because the other RRM2 structures have a Cys in this position that does not alter the equivalent Phe positions, those Phe conformations are such that the pore is occluded in the RRM2 structures (Figures 8A,B, S3A−C, and S4A−C). Therefore, the open channel is linked to the Cys versus Tyr difference observed in helix D. That this pore is in the immediate vicinity of the iron binding site of hp53R2, and is not seen in m/hRRM2, is a second explanation for why hp53R2 is 158-fold more susceptible to the iron chelator, deferoxamine mesylate, than hRRM2 is (*13*). Aside from possibly conferring increased susceptibility to iron chelators, the channel may play a role in the regulation of the enzyme, though much has yet to be determined about the hp53R2

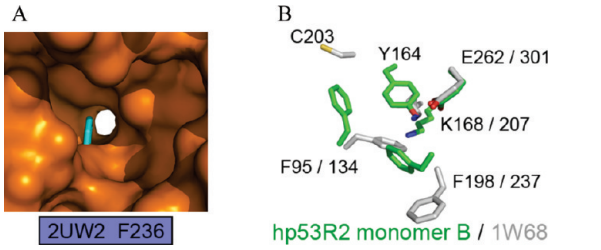

FIGURE 8: (A) View of the hp53R2 monomer A pore with 2UW2 phenylalanine 236 overlaid to show how this residue occludes the pore in both hRRM2 and mRRM2 structures. (B) View of hp53R2 monomer B overlaid with 1W68 displaying the conformational changes at specific phenylalanines that lead to the pore occlusion in the hRRM2 and mRRM2 structures, but not the hp53R2 structure. The conformational changes can be traced back to the sequence switch from C202 and C203 in hRRM2 and mRRM2, respectively, to Y164 in hp53R2.

regulatory pathway. Site-directed mutagenesis specific to residues in the tunnel region could offer insight into the physiological importance of this region.

Structural Insights and Potential Anticancer Relevance. RNR is paramount for cancer survival and is a validated target for anticancer agents. There are currently many RNR-targeting anticancer molecules in the clinic or in various clinical trials. However, the broad specificity of many such RNR inhibitors remains a major shortcoming. The idea of inhibiting the RNR small subunits selectively is one with much appeal and momentum, because different cancers use the two dNTP-producing pathways differently. For example, inhibiting p53R2 but not R2 can specifically target tumors that overexpress p53R2. Further, the inactivation of hp53R2-dependent DNA synthesis will activate p53-dependent apoptosis (*8*, *9*).

Several insights have been gleaned from the hp53R2 crystal structure. Three major structural regions have been highlighted to impart major differences between the iron-protective environments, in addition to an enzyme-spanning pore that passes directly to one side of the hp53R2 iron core. With >80% sequence identity between the two subunits, the differences observed in the X-ray crystal structures are differences that could not have been clearly or readily identified by other methods.

The most likely region to be exploited from a rational drug design perspective is the channel spanning each monomer. Figure S1 of the Supporting Information shows that this region is exposed in both the monomeric and dimeric hp53R2 structures. In silico inhibitor screening efforts that limit the search parameters to this pocket could first filter molecules on the basis of size and geometric constraints and then optimize the identified subset of compounds on the basis of charge properties. These criteria could exclude a large number of inhibitor-like candidates and identify a manageable subset for subsequent in vitro inhibition assays. Therefore, the hp53R2 crystal structure provides a template for the in silico inhibitor screening effort that will impact the development of RNR small subunit specific anticancer therapeutics.

Biological Significance. hp53R2, the first p53R2 X-ray crystal structure, exhibits many distinct structural features not reported before in the m/hRRM2 structures. The sequence switch from C203 and C202 in m- and hRRM2, respectively, to Y164 in hp53R2 results in a dramatic change in the surrounding phenylalanine conformations, creating a central channel through hp53R2, not seen in reported homologous structures. This feature helps to explain the increased susceptibility of hp53R2 to iron-sequestering

deferoxamine mesylate (*13*). Additionally, in hp53R2, the communication between the N-terminal swivel residues, and opposite helices B and D, allows two different conformations that alternatively swivel at residues R40 and R41, as well as K151 and R152. These conformations are structural evidence of a possible gating mechanism in iron assimilation. Though the swivel can occur at the equivalent N-terminal positions in the mRRM2 structures, it does not lead to the far-sweeping differences seen in hp53R2 due to sequence variations. That helix B can exist in an open conformation in hp53R2 implies a mechanism of iron incorporation different from those of homologous RRM2 structures and offers further evidence to bolster the observation that hp53R2 binds iron less well and that it is more susceptible to the iron-chelating deferoxamine mesylate (*13*). This also lends insight into a possible role for iron availability and occupancy relative to hp53R2 pathway regulation. Though the full biological cascade and control mechanisms relating to hp53R2 have yet to be determined, it is possible that the enzyme is under some form of iron-dependent activation and/or repression. For the first time, the structural differences are presented between the two mammalian small subunits. These insights pave the way for understanding the biological function, regulation mechanism, and development of selective inhibitors of these RNR small subunits.

ACKNOWLEDGMENT

Portions of this research were conducted at the Stanford Synchrotron Radiation Laboratory (SSRL), a national user facility operated by Stanford University on behalf of the U.S. Department of Energy, Office of Basic Energy Sciences. The SSRL Structural Molecular Biology Program is supported by the Department of Energy, Office of Biological and Environmental Research, and by the National Institutes of Health, National Center for Research Resources, Biomedical Technology Program, and the National Institute of General Medical Sciences. The Advanced Light Source is supported by the Director, Office of Science, Office of Basic Energy Sciences, of the U.S. Department of Energy under Contract DE-AC02-05CH11231.

SUPPORTING INFORMATION AVAILABLE

Data statistics and graphics that further detail important structural features of hp53R2 in comparison with the homologous mammalian structures described in the text and discussion of assumptions used in the homologous structure comparisons. This material is available free of charge via the Internet at http://pubs.acs.org.

REFERENCES

1. Jordan, A., and Reichard, P. (1998) Ribonucleotide reductases. *Annu. Rev. Biochem. 67*, 71–98.
2. Stubbe, J., and Riggs-Gelasco, P. (1998) Harnessing free radicals: Formation and function of the tyrosyl radical in ribonucleotide reductase. *Trends Biochem. Sci. 23*, 438–443.
3. Stubbe, J. (2003) Di-iron-tyrosyl radical ribonucleotide reductases. *Curr. Opin. Chem. Biol. 7*, 183–188.
4. Chabes, A., and Thelander, L. (2000) Controlled protein degradation regulates ribonucleotide reductase activity in proliferating mammalian cells during the normal cell cycle and in response to DNA damage and replication blocks. *J. Biol. Chem. 275*, 17747–17753.
5. Filatov, D., and Thelander, L. (1995) Role of a proximal NF-Y binding promoter element in S phase-specific expression of mouse ribonucleotide reductase R2 gene. *J. Biol. Chem. 270*, 25239–25243.
6. Liu, X.; et al. (2004) Nuclear factor Y regulation and promoter transactivation of human ribonucleotide reductase subunit M2 gene in gemcitabine resistant KB clone. *Biochem. Pharmacol. 67*, 1499–1511.
7. Chabes, A. L., Bjorklund, S., and Thelander, L. (2004) S phase-specific transcription of the mouse ribonucleotide reductase R2 gene requires both a proximal repressive E2F-binding site and an upstream promoter activating region. *J. Biol. Chem. 279*, 10796–10807.
8. Tanaka, H.; et al. (2000) A ribonucleotide reductase gene involved in a p53-dependent cell-cycle checkpoint for DNA damage. *Nature 404*, 42–49.
9. Yamaguchi, T.; et al. (2001) p53R2-dependent pathway for DNA synthesis in a p53-regulated cell cycle checkpoint. *Cancer Res. 61*, 8256–8262.
10. Kimura, T.; et al. (2003) Impaired function of p53R2 in Rrm2b-null mice causes severe renal failure through attenuation of dNTP pools. *Nat. Genet. 34*, 440–445.
11. Guittet, O.; et al. (2001) Mammalian p53R2 protein forms an active ribonucleotide reductase in vitro with the R1 protein, which is expressed both in resting cells in response to DNA damage and in proliferating cells. *J. Biol. Chem. 276*, 40647–40651.
12. Zhou, B.; et al. (2005) A dityrosyl-diiron radical cofactor center is essential for human ribonucleotide reductases. *Mol. Cancer Ther. 4*, 1830–1836.
13. Shao, J.; et al. (2004) In vitro characterization of enzymatic properties and inhibition of the p53R2 subunit of human ribonucleotide reductase. *Cancer Res. 64*, 1–6.
14. Otwinowski, Z., and Minor, W. (1997) Processing of X-ray diffraction data collected in oscillation mode. *Methods Enzymol. 276*, 307–326.
15. Strand, K. R.; et al. (2004) Crystal structural studies of changes in the native dinuclear iron center of rionucleotide reductase protein R2 from mouse. *J. Biol. Chem. 279*, 46794–46801.
16. Kissinger, C. R., Gehlhaar, D. K., and Fogel, D. B. (1999) Rapid automated molecular replacement by evolutionary search. *Acta Crystallogr. D55*, 484–491.
17. Brunger, A. T.; et al. (1998) Crystallography & NMR system: A new software suite for macromolecular structure determination. *Acta Crystallogr. D54*, 905–921.
18. Emsley, P., and Cowtan, K. (2004) Coot: Model-building tools for molecular graphics. *Acta Crystallogr. D60*, 2126–2132.
19. Kauppi, B.; et al. (1996) The three-dimensional structure of mammalian ribonucleotide reductase protein R2 reveals a more-accessible iron-radical site than *Escherichia coli* R2. *J. Mol. Biol. 262*, 706–720.